Advanced Electronic Materials

ADVANCED ELECTRONIC MATERIALS Open Access

www.advelectronicmat.de

RESEARCH ARTICLE OPEN ACCESS

Ferroelectric Behavior of Micro- to Submicron-Scale HZO Capacitors: Impact of the Perimeter-to-Area Ratio

Lucian Trupina[1] | Stefan Neatu[1] | Lucian Pintilie[1] | Lucia Nicoleta Leonat[1] | Stavros Kitsios[2] | Stefania Skorda[2,3,4] | Alexandros El Sachat[2] | Polychronis Tsipas[1,2] | Alexander Flasby[5] | Laura Bégon-Lours[5] | Athanasios Dimoulas[1,2]

[1]National Institute of Materials Physics, Magurele, Romania | [2]National Centre for Scientific Research DEMOKRITOS, Athens, Greece | [3]Institute of Nanoscience and Nanotechnology, National Center for Scientific Research "Demokritos, Athens, Greece | [4]Department of Applied Physics, National Technical University of Athens, Athens, Greece | [5]Integrated Systems Laboratory, D-ITET, ETH Zürich, Zürich, Switzerland

Correspondence: Lucian Trupina (lucian.trupina@infim.ro)

Received: 15 December 2025 | **Revised:** 20 April 2026 | **Accepted:** 22 May 2026

Keywords: conductive AFM | edge-dominated switching | nanoscale capacitors | scaling effects

ABSTRACT

The aggressive scaling of electronic devices has brought ferroelectric materials to the forefront of nanoscale research, where lateral dimensions strongly influence switching dynamics and device performance. In this context, W/ $Hf_{0.5}Zr_{0.5}O_2$/ p-Ge capacitors with top electrode sizes ranging from 10 μm down to 0.1 μm are investigated using conductive atomic force microscopy (C-AFM). Frequency-dependent measurements reveal that peak switching currents (I_{sw}) increase with sweep rate, yet the total switched charge remains nearly constant, consistent with full polarization reversal in micro- and submicron devices. Positive-Up-Negative-Down (PUND) analysis further isolates the switching current, allowing reconstruction of polarization–voltage (*P*--*V*) loops and quantification of remnant polarization. The smallest devices (0.01 μm^2) exhibit switching currents below the detection threshold due to parasitic capacitance, masking intrinsic ferroelectric behavior. In contrast, submicron capacitors display an apparent increase of remanent polarization attributed to the larger perimeter-to-area ratio, emphasizing the role of edge-dominated switching. Together, these findings establish C-AFM as a powerful, spatially resolved technique for probing ferroelectric switching in realistic device geometries, providing essential insights for non-volatile memory and neuromorphic applications.

1 | Introduction

The relentless pursuit of miniaturization in modern electronics has made the characterization of material properties at the nanoscale not merely a scientific curiosity but a technological imperative. As device dimensions shrink to the nanometer scale, bulk material properties no longer adequately describe the behavior of active components. At this reduced length scale, local heterogeneities, grain boundaries, defects, and surface effects become dominant, profoundly influencing device performance and reliability [1]. Lateral scaling of ferroelectric two-terminal devices, such as ferroelectric capacitors (FeCAPs), ferroelectric tunnel junctions (FTJs) and ferroelectric diodes (FD) present additional challenges [2]. Restrictions in ferroelectric domain wall motion and switching due to grain boundaries in poly-crystalline films may become critical, reducing device speed. Moreover, the accessibility of many intermediate states, therefore, the operation in a multistate analog memristor mode [3] is not guaranteed in laterally small devices. Experiments with nanoscale FTJ or FD devices are needed to properly address these issues.

Most research test structures are fabricated at the tens-of-micrometers scale (~10–50 μm lateral size) and measured using

conventional micrometer-sized probes. Results obtained from submicron ($0.5 \times 0.5\ \mu m^2$ area) MFM capacitors integrated in the BEOL of CMOS [4] are encouraging, showing no degradation of ferroelectric characteristics (e.g., P_r) and improved endurance, attributed to reduced defect density. Devices with lateral dimensions in the range 500 nm down to 14 nm [5] show a reduction of coercive field with scaling, benefiting cycling endurance without adverse effects on the fast operation at the nanosecond scale. During the materials development stage, devices with areas below $1 \times 1\ \mu m^2$ typically require narrow metal lines connected to larger probe pads over a spacer layer (oxide), defined by lithography and etching; this adds fabrication complexity and cost. The large parasitic capacitance of such probe pads placed in parallel with the small device capacitance can mask the intrinsic switching response. Consequently, techniques capable of providing spatially resolved measurements with nanometer-scale precision are essential for both fundamental research and industrial applications. Piezoresponse force microscopy (PFM) is widely used to investigate ferroelectricity at the nanoscale by imaging domains and recording local hysteresis loops [6, 7]. However, PFM signals can be influenced by extrinsic effects such as surface charging, ionic motion, or electrochemical activity, making the identification of ferroelectric switching challenging [8–13]. To overcome these limitations, we employ conductive atomic force microscopy (C-AFM), which directly measures current under applied bias and enables both current mapping and local *I–V* spectroscopy [14]. From these data, polarization–voltage (*P–V*) characteristics can be reconstructed, allowing extraction of key ferroelectric parameters such as remnant polarization and coercive field. Moreover, C-AFM can distinguish between regions dominated by leakage current and those exhibiting ferroelectric switching by analyzing the local *I–V* curves, their dependence on voltage sweep rate and frequency, the stability of successive cycles, and the spatial distribution of current [15].

A distinct advantage of C-AFM is its applicability to real device geometries, including submicron capacitors where the increased surface-to-volume ratio amplifies interfacial and edge effects, influencing the switching behavior. Recently, the nano-positive up negative down (nano-PUND) method was introduced as an advanced approach to probe ferroelectric switching currents at the nanoscale in HfO_2-based thin films [16]. Demonstrated on bare films without top electrodes, it enabled the extraction of switching currents while suppressing capacitive artifacts. Yet, because the switched area was only estimated indirectly, the quantitative values of remnant polarization remain uncertain.

Here, we employ conductive atomic force microscopy (C-AFM) on fully fabricated W/HZO/p-Ge capacitors with a wide range of top electrode dimensions, from 10 μm-diameter circles down to square patterns with 0.1 μm lateral size. Probing the structures directly through the top electrodes allows us to capture ferroelectric switching in realistic device geometries, bridging the gap between nanoscale investigations and practical operating conditions. The selection of the W/HZO/p-Ge stack is crucial, as the thermal expansion mismatch of the Ge substrate induces a beneficial tensile strain that stabilizes the ferroelectric orthorhombic phase. Unlike Si-based systems, the instability of germanium oxides yields a clean, abrupt interface, minimizing voltage drops and depolarization fields in HZO ultrathin films (< 10 nm) [17, 18]. Furthermore, the narrow bandgap and high carrier concentration of Ge provide superior polarization charge screening, which directly influences the wake-up effect and enhances device endurance compared to Si counterparts. In addition, the use of Ge provides a viable route to the realization of Ge-based ferroelectric field-effect transistors (FeFETs) [19].

By correlating local electrical spectroscopy with surface-sensitive XPS, we elucidate how electrode surface chemistry influences the magnitude of locally measured switching current. Our investigation provides an analysis of HZO switching dynamics by quantifying the frequency dependence and *P–V* characteristics, alongside characterizing the wake-up behavior. Crucially, we establish the non-linear scaling of current and charge density with electrode area, confirming that the ratio between the perimeter and the electrode area (*P/A*) and edge effects strongly contribute to the measured polarization in submicron capacitors. Our results highlight the importance of lateral scaling effects on device performance and validate C-AFM as a robust, device-relevant methodology with direct implications for ferroelectric memory and neuromorphic applications.

2 | Results and Discussion

2.1 | Structural and Chemical Properties of Substrates and HZO Films

To assess the structural and chemical quality of the samples, the substrate surface structure, thin film composition, and surface chemical properties were analyzed using RHEED together with in situ and ex situ XPS. The Ge(100) substrate, cleaned by UHV annealing, exhibited a well-defined (2×1) surface reconstruction; the RHEED image and detailed analysis are provided in (Figure S1). In situ XPS was performed immediately after HZO deposition, providing a pristine stoichiometric baseline and avoiding air exposure. Ex situ XPS allowed precise examination of the W electrode surface after deposition and subsequent processing, allowing detailed investigation of tungsten oxidation states, as tungsten is prone to oxidation when exposed to air. The HZO layer exhibited a near-stoichiometric Hf/ Zr composition, ensuring the formation of the ferroelectric orthorhombic phase upon rapid thermal annealing (Figure S2). Ex situ measurements on regions containing W electrodes revealed the presence of W, O, Hf, Zr, and minor surface carbon contamination, with no detectable foreign elements. High-resolution spectra showed multiple tungsten oxidation states (W^{6+}, W^{5+}, W^{4+}, and metallic W^0), indicating the presence of mixed WO_{3-x} regions, consistent with earlier reports [20–22] (Figures S3 and S4). These oxidized regions are intrinsic to the electrode surface and play a key role in the local conductivity variations observed by C-AFM measurements, as discussed later.

2.2 | Ferroelectric Properties of Micron-Scale Capacitors

Conventional electrical measurements of 50×50 and $10 \times 10\ \mu m^2$ W/HZO/p-Ge capacitors confirmed ferroelectric behavior, with an average remnant polarization $P_r \approx 22\ \mu C \cdot cm^{-2}$ (Figure 1a,b). The *P-V* hysteresis loops were well-defined for large devices, while smaller capacitors showed higher current noise, as seen

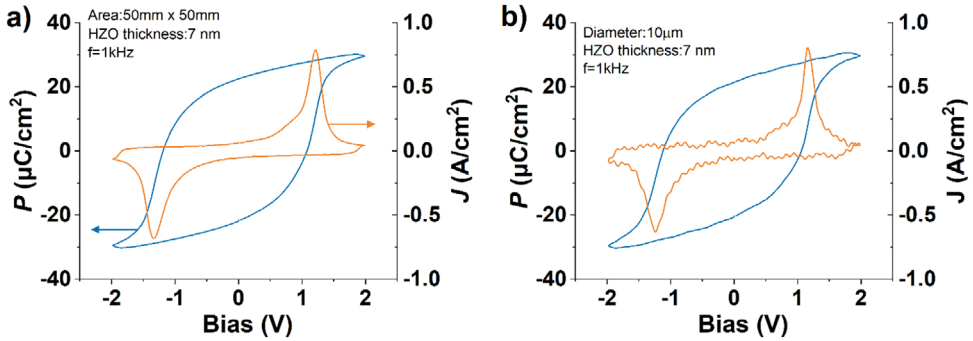

FIGURE 1 | Ferroelectric characteristics measured by a conventional thin-film ferroelectric tester. *P–V* (blue) and switching displacement current *I–V* curves (orange–brown) for (a) 50×50 μm^2 and (b) 10×10 μm^2 capacitors.

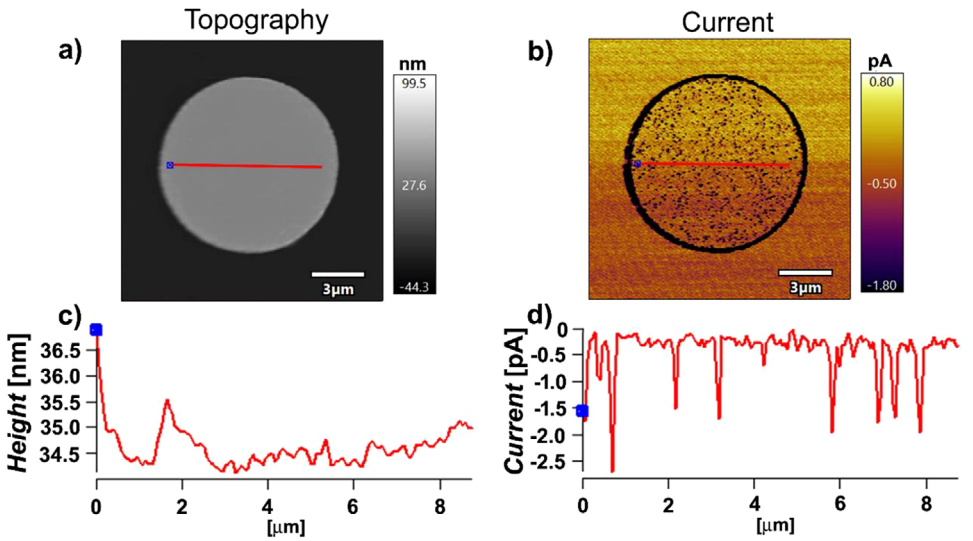

FIGURE 2 | (a) AFM topography images of a 10 μm-diameter tungsten top electrode, recorded over 15×15 μm^2 scan area. (b) Corresponding C-AFM current maps acquired under a −0.5 V bias over the same area as in (a). (c,d) Line profiles of topography and current, extracted along the red lines shown in (a,b), respectively.

in the switching displacement current *I–V* curves of Figure 1b. This behavior highlights the limitations of macroscopic testing for scaled devices and the need for localized nanoscale probing.

The topography images of a 10 μm-diameter W electrode, acquired by AFM, revealed smooth surfaces with a root-mean-square roughness (RMS) of 2.2 nm (Figure 2a). Simultaneously recorded current map under a −0.5 V bias (Figure 2b) revealed spatial variations in local conductivity. Notably, these variations did not correlate with the electrode surface morphology (Figure 2c,d), suggesting that they originate from local variations in the chemical state of the electrode rather than topographic artifacts. Additional measurements performed under vacuum and at higher applied bias (2.7 V) confirmed that the conductivity inhomogeneities persist, indicating they are intrinsic to the electrode surface rather than caused by adsorbates or ambient moisture (see Figure S5).

The current enhancement observed at electrode edges in C-AFM maps originates from geometric effects at the electrode boundaries, which result in both a stronger local electric field and improved mechanical/electrical contact between the tip and the sample [23]. As shown in Figure 2b, this edge-induced field concentration promotes higher local current through the HZO layer. Beyond geometric effects, spatial variations in tungsten oxidation also influence the local electrical response. Regions containing higher-valence W oxides exhibit lower conductivity, whereas partially reduced or metallic W provides more conductive pathways. This correlation between electrode surface chemistry and nanoscale conduction highlights the impact of tungsten oxidation on the nanoscale electrical response of the device.

2.3 | Nanoscale *I–V* Characterization and Wake-Up Effects

To investigate the origin of these spatial differences, *I–V* characteristics were recorded in well-defined locations that showed distinct current levels on the C-AFM map (Figure 2b, bright and small dark regions). The AFM tip was positioned with the "Pick a Point" function of the MFP-3D SA system, and voltage sweeps between −2 and +2 V at 1 Hz were applied. The resulting *I-V* curves, averaged over five consecutive cycles

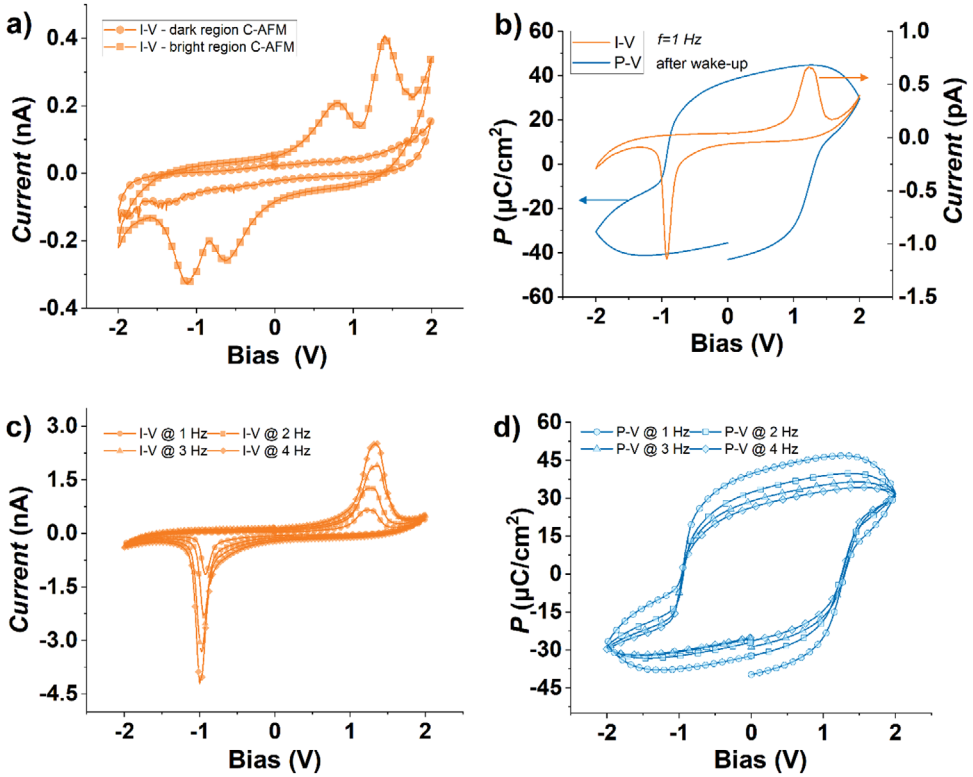

FIGURE 3 | (a) *I–V* characteristics measured by C-AFM at two specific locations: the curve with square markers corresponds to the region with higher current levels, while the curve with circular markers represents the region with lower current levels. (b) The *P–V* hysteresis loop (blue curve) and the *I–V* characteristic (orange–brown curve) measured after the wake-up process in the region with higher current levels. (c) The *I–V* characteristics and (d) *P–V* hysteresis loops measured in the region with higher current levels at 1, 2, 3, and 4 Hz after the wake-up process.

at the same location, are shown in Figure 3a. At the site with suppressed current, the *I–V* curve was nearly flat (indicated by the circular markers in Figure 3a), indicating the absence of switching currents within the applied voltage range. However, when higher voltages were applied (see Figure S6), polarization reversal could still be induced, consistent with the presence of tungsten oxides identified by XPS. By contrast, the region with enhanced conductivity exhibited higher current levels and a characteristic bipolar curve with double peaks (indicated by square markers in Figure 3a), typical of polarization-dependent displacement currents associated with domain switching.

The presence of these double peaks is a characteristic feature of pristine HZO films [24]. This double-peak structure reflects the pinched loop typical of the as-grown state but does not imply the existence of a true antiferroelectric phase. Following electrical cycling, the ferroelectric response improved significantly due to the wake-up effect. This process is largely attributed to the redistribution of mobile oxygen vacancies, which annihilate at the interfaces under repeated cycling, thereby reducing the internal field that pins the ferroelectric domains [25]. As shown in Figure 3b, both the *I–V* and reconstructed *P–V* loops became more symmetric and exhibited enhanced switching currents after 1000 electrical cycles. This improved behavior confirms that cycling stabilizes the ferroelectric orthorhombic phase by reducing internal bias fields and enabling the activation of previously unswitched domains.

Frequency-dependent *I–V* measurements further revealed an increase in peak switching current with frequency, consistent with charge conservation during fast pulse transitions. As shown in Figure 3c, the switching currents increase with frequency, and the coercive voltage shifts slightly toward higher values. This behavior is expected because the total switched charge Q_{sw} is ideally constant, as it is a material property. Since Q_{sw} corresponds to the time integral of the switching current, when the voltage is applied over a shorter time interval (at a higher frequency), the current must increase accordingly to maintain the same total charge. In other words, a faster switching process results in a higher peak current. Theoretically, the four *P–V* loops shown in Figure 3d should overlap and exhibit the same $2P_r$ value. However, at low frequencies, leakage currents become more significant relative to the switching displacement current, leading to distortions in the measured current. As a result, the integrated polarization is affected, and the loop shape deviates from the ideal behavior.

2.4 | Local Polarization Switching Across Entire Electrodes

To confirm the applicability of this local method to real devices, single-pulse experiments showed that a voltage pulse applied locally through the AFM tip could induce uniform polarization reversal across the entire area of a 10 μm-diameter electrode (Figure 4), validating the ability of C-AFM to probe devices under

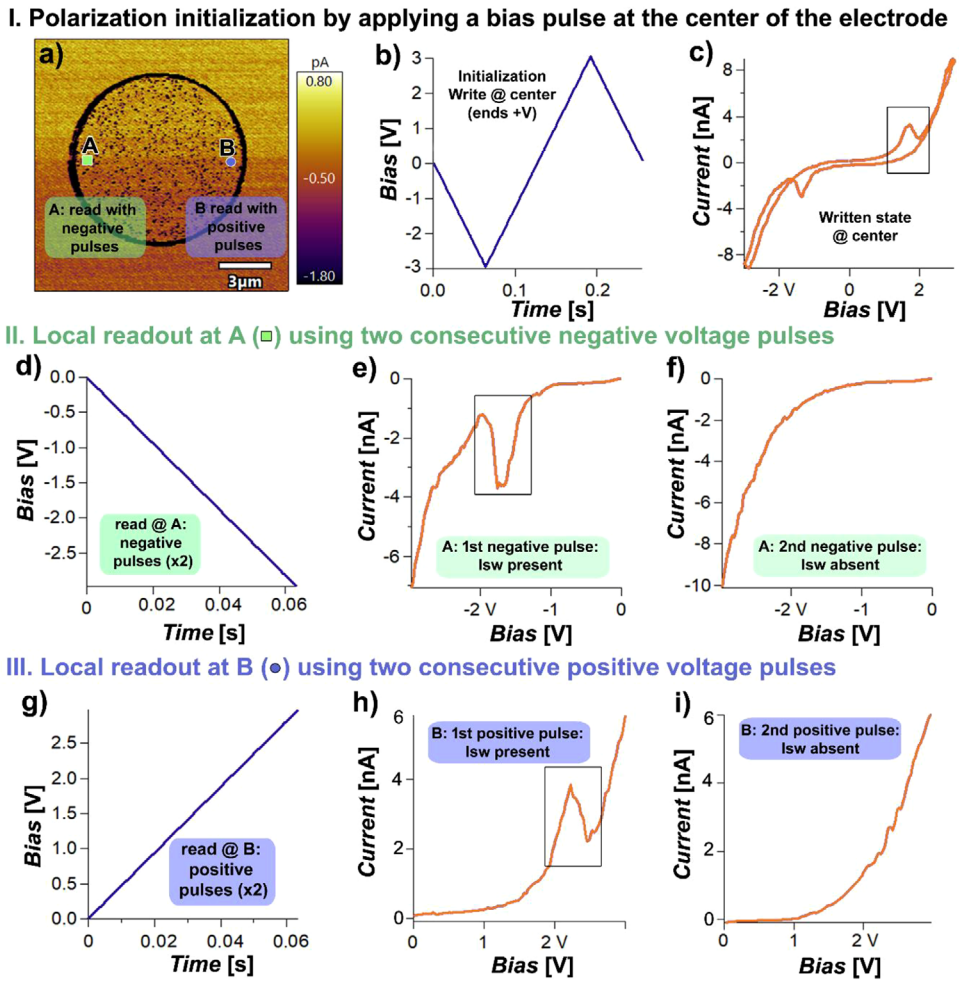

FIGURE 4 | (a) C-AFM current map of a 10 µm-diameter capacitor, indicating two local readout positions: point A (green square, negative pulses) and point B (blue circle, positive pulses). (b) Polarization initialization by a full voltage cycle (-3 to +3 V, 4 Hz) applied at the electrode center, with the corresponding *I–V* curve shown in (c). (d) Readout protocol at point A, where the same negative voltage pulse is applied twice consecutively, and the current is recorded after each pulse; the resulting *I–V* curves are shown in (e,f). (g) Readout protocol at point B, where the same positive voltage pulse is applied twice consecutively, and the current is recorded after each pulse; the resulting *I–V* curves are shown in (h,i). The absence of switching during the second pulse at both locations demonstrates device-scale polarization reversal under the entire electrode, consistent with the near-equipotential behavior of the highly conductive W top electrode.

realistic conditions. First, a full voltage cycle from − 3 to + 3 V (Figure 4b) was applied at the center of the electrode, initializing the capacitor in the upward polarization state. Subsequently, two consecutive negative pulses were applied at point A, located near the electrode edge (Figure 4a). Point A is marked in Figure 4a by a green square, while point B, marked by a blue circle, corresponds to the location where positive voltage pulses are applied. The first pulse induced a clear switching current (Figure 4e), while the second pulse produced no switching (Figure 4f), demonstrating that the polarization at point A had been fully reversed to the downward state by the first pulse. We then moved the AFM tip to the diametrically opposite edge (point B in Figure 4a) and applied two consecutive positive pulses. Again, switching was observed only during the first pulse (Figure 4h), while the second pulse produced no switching (Figure 4i). Consistent switching observed in readout signals recorded at 1, 3, and 5 µm from the center confirmed large-area polarization reversal. Together, these widely separated stimuli and electrical readouts are consistent with device-scale polarization reversal under the electrode, i.e., far beyond the immediate tip-sample contact. The physical origin of this extended switching stems from the high conductivity of the 30 nm W electrode, which rapidly redistributes the applied potential and establishes an equipotential surface. A simple upper-bound estimate shows that the lateral voltage drop across a 5 µm radius electrode is negligible under our conditions ($\Delta V < 1$ mV for the measured picoampere-level currents and the low sheet resistance of W), so the normal field in the HZO is essentially uniform across the electrode area. Nevertheless, local variations in interface chemistry may cause initial nucleation beneath the tip, followed by gradual lateral domain expansion until complete switching is achieved. Thus, the reversal process combines global field-driven activation with local domain propagation. Given the high conductivity of the W electrode, the uniform electric field distribution is expected to dominate the switching process, while local domain propagation likely contributes only to the initial nucleation and short-range lateral expansion beneath the tip. Although isolated unswitched domains cannot be definitively excluded, their presence is unlikely based on the uniform

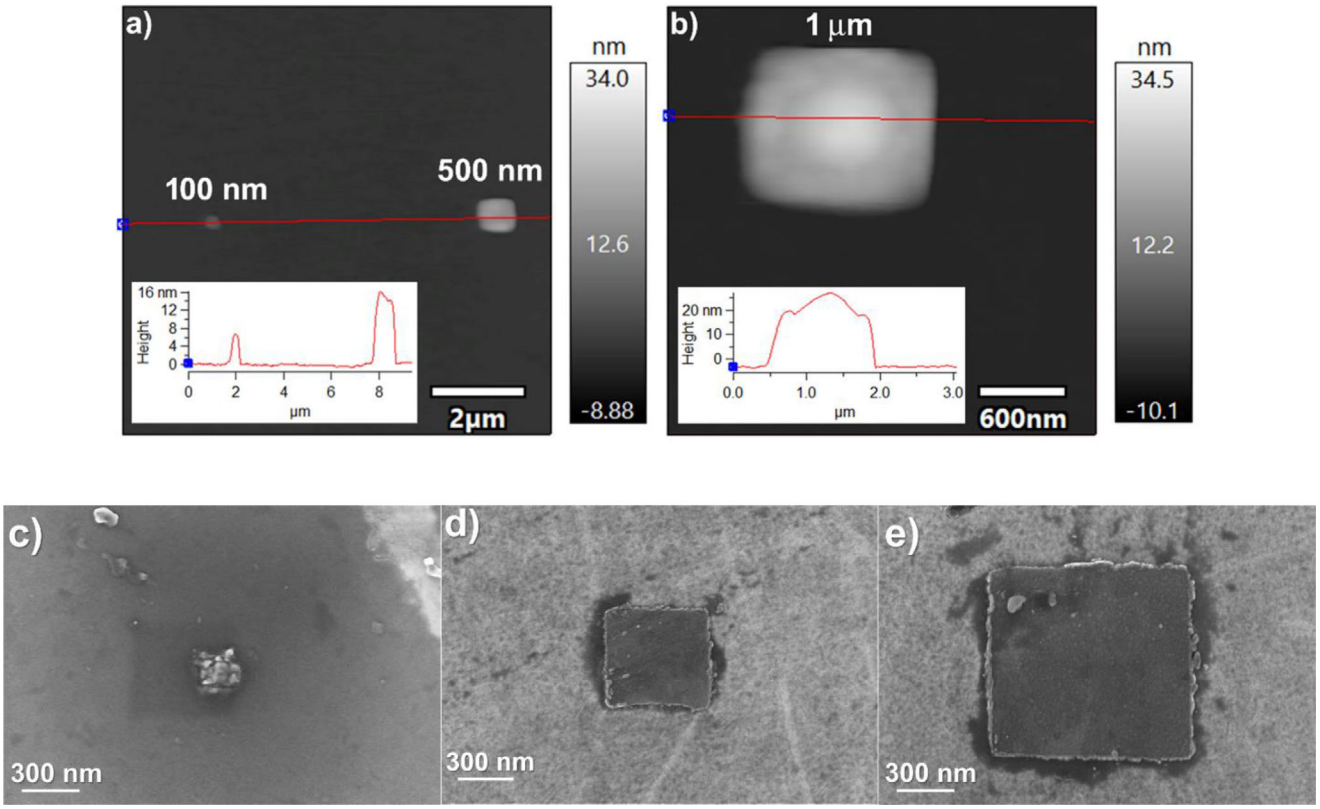

FIGURE 5 | AFM and SEM images of nanoscale capacitors. The figure shows square capacitors with nominal lateral dimensions of 0.1, 0.5, and 1 µm. Panels (a,b) present AFM images of: (a) 0.1 and 0.5 µm devices, while (b) shows the 1 µm device. Insets display cross-sectional profiles extracted from the AFM topography. Panels (c–e) show the corresponding SEM images of the electrodes with nominal lateral dimensions of 0.1, 0.5, and 1 µm, respectively.

switching signals. Ideally, PFM phase imaging through the top electrode would provide direct confirmation of uniform domain switching. However, such imaging was not feasible in this case because the 30 nm-thick metallic W electrode introduces strong mechanical damping, and the piezoelectric response of HZO is intrinsically weak.

2.5 | Scaling Effects on Submicron Capacitors

We next investigated submicron capacitors with a 12 nm thick HZO layer fabricated by electron-beam lithography, with nominal lateral dimensions down to 0.1 µm (nominal area 0.01 µm^2, see Figure 5). High-resolution atomic force microscopy images of nanoscale capacitors with nominal lateral dimensions of 0.1, 0.5, and 1 µm are shown in Figure 5a,b, respectively. Current maps were collected under identical non-perturbative conditions as those used for the 10 µm diameter capacitor (Figure S8 for detailed discussion on the visibility of static contrast and scaling limits). Cross-sectional line profiles, shown as insets, reveal that the measured electrode dimensions deviate from the nominal design values. This discrepancy primarily results from variations introduced during the etching process and from inherent limitations of AFM imaging. In particular, the finite curvature of the AFM tip and its progressive wear during repeated scans reduce lateral resolution, leading to an overestimation of feature sizes. Additionally, edge roughness limits the precision in determining electrode areas. Therefore, the actual capacitor area used for effective polarization calculations was determined from high-resolution SEM images (Figure 5c–e) using Gwyddion Grain Analysis via manual thresholding. For square electrodes with nominal side lengths of 1 and 0.5 µm, the measured areas were 1.03 ± 0.02 and 0.26 ± 0.01 µm^2, respectively; these values were used in the $2P_r$ calculations.

The *I*–*V* curves were first measured at sweep frequencies of 1, 2, 3, and 4 Hz to evaluate the frequency dependence of the peak switching current. Subsequently, Positive-Up-Negative-Down (PUND) measurements were performed to isolate the switching current component and extract effective polarization. For the largest capacitor (1.03 µm^2), the maximum switching current was about 18–20 pA (Figure 6a), whereas for the smaller 0.26 µm^2 capacitor, the peak current decreased to approximately 8–10 pA (Figure 6b), both measured at 4 Hz. This decrease is expected, as fewer ferroelectric domains contribute to switching current in the smaller device.

Notably, for the smallest device (0.01 µm^2; Figure 6c), the ferroelectric switching peaks are no longer discernible, and the current response is entirely dominated by the linear, non-switching capacitive component [26]. Based on a simple linear scaling with electrode area (0.01 × reduction), the expected peak switching current would be approximately 0.2 pA. However, this extremely weak signal is completely obscured by the much larger non-switching background current (~40 pA), mainly originating from the parasitic capacitance of the probe and surrounding circuitry.

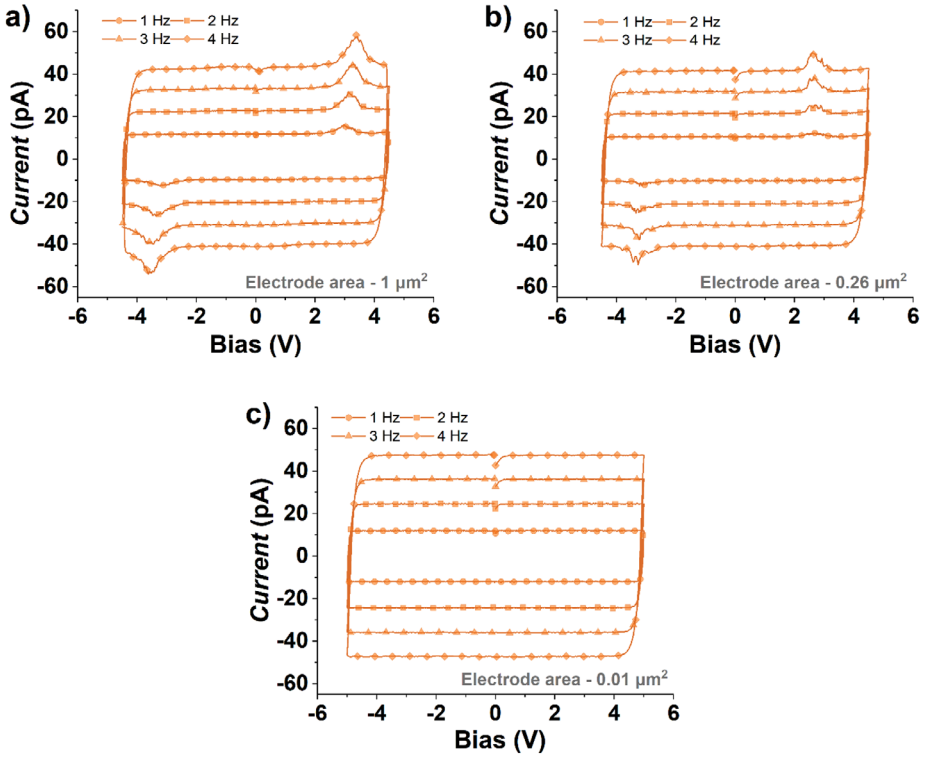

FIGURE 6 | *I–V* characteristics for three different electrode areas: (a) 1 μm², (b) 0.26 μm², and (c) 0.01 μm² measured at four distinct frequencies 1, 2, 3, and 4 Hz.

As a result, intrinsic ferroelectric behavior cannot be resolved at this lateral scale.

In Figure 6a,b, the *I–V* curves of the 1.03 and 0.26 μm² capacitors across four sweep frequencies show a clear increase in current with frequency, accompanied by a slight shift of the coercive voltage toward higher values. Notably, the integrated switching charge remains nearly constant across frequencies, around $(1.6 \pm 0.1) \times 10^{-13}$ C for positive pulses (and slightly lower for negative ones), confirming that polarization reversal is fully completed within the applied voltage range and that the total switched charge is unaffected by the voltage ramp at these slow sweep rates (1–4 Hz).

In addition to switching analysis, the same set of multi-frequency *I–V* curves was also used to extract the parasitic capacitance (C_{par}) and leakage current (I_{leak}). To quantitatively assess the background that limits the visibility of switching in the smallest devices, the setup-dominated parasitic (C_{par}) was rigorously decoupled from leakage using a two-frequency protocol evaluated in the non-switching voltage regime (see Note S6). This analysis yielded a tightly bounded, area-independent parasitic capacitance of approximately 0.59 pF (0.60 pF for the 1.03 μm² capacitor and 0.58 pF for the 0.26 μm² capacitor), confirming that the background is entirely dominated by the probe and surrounding circuitry. This intrinsic capacitance dictates the magnitude of the measured current plateaus ($\approx C_{par} \cdot dV/dt$), which scale from ~ 10–12 pA at 1 Hz to ~ 40–50 pA at 4 Hz for the applied bias 10 V_{pp} ramps. Beyond this deterministic background, the detection limit is set by residual current fluctuations on the plateau. Using a robust MAD-to-σ estimator in a strict [+ 1, + 2] V window, we determined a limit of detection $I_{LOD}(3\sigma) \approx$ 0.3–0.4 pA (see Note S5). Given that the switching current scales linearly with electrode area, the 0.01 μm² capacitor is expected to produce a peak of only ~ 0.2 pA at 4 Hz. This signal is not only below the I_{LOD}, but it represents a mere 0.4% contribution to the total measured current (50 pA). Consequently, the intrinsic ferroelectric peaks are completely masked by the overwhelming setup-dominated background and the associated system noise, explaining their absence in the raw data for the 0.01 μm² capacitor.

2.6 | Edge-Induced Enhancement of Apparent Polarization and Implications for Nanoscale Probing

PUND measurements on laterally scaled capacitors (Figure 7) enable the isolation of switching from non-switching contributions and the quantitative reconstruction of polarization–voltage loops. Switching charge was extracted using the model-based background correction described in Section 4 and SI Note S7. Figures 7a,b display the complete PUND pulse sequences recorded on the 1.03 μm² and 0.26 μm² capacitors, respectively. In Figure 7c,d, the background-corrected switching current is plotted as the mean trace with a shaded ± standard deviation (SD) band (1 μm²: $n = 7$; 0.26 μm²: $n = 4$ *I–V* cycles). For each cycle, I_{sw} was numerically integrated over time to yield the switched charge Q_{sw}, which was then used to reconstruct the P-V loops (across-runs mean ± SD) shown in Figure 7e,f).

The PUND analysis reveals a pronounced size dependence of the effective remanent polarization ($2P_r$). For each device (area 1.03 and 0.26 μm²), multiple PUND cycles acquired at the same location were analyzed. $2P_r$ was obtained from the stabilized

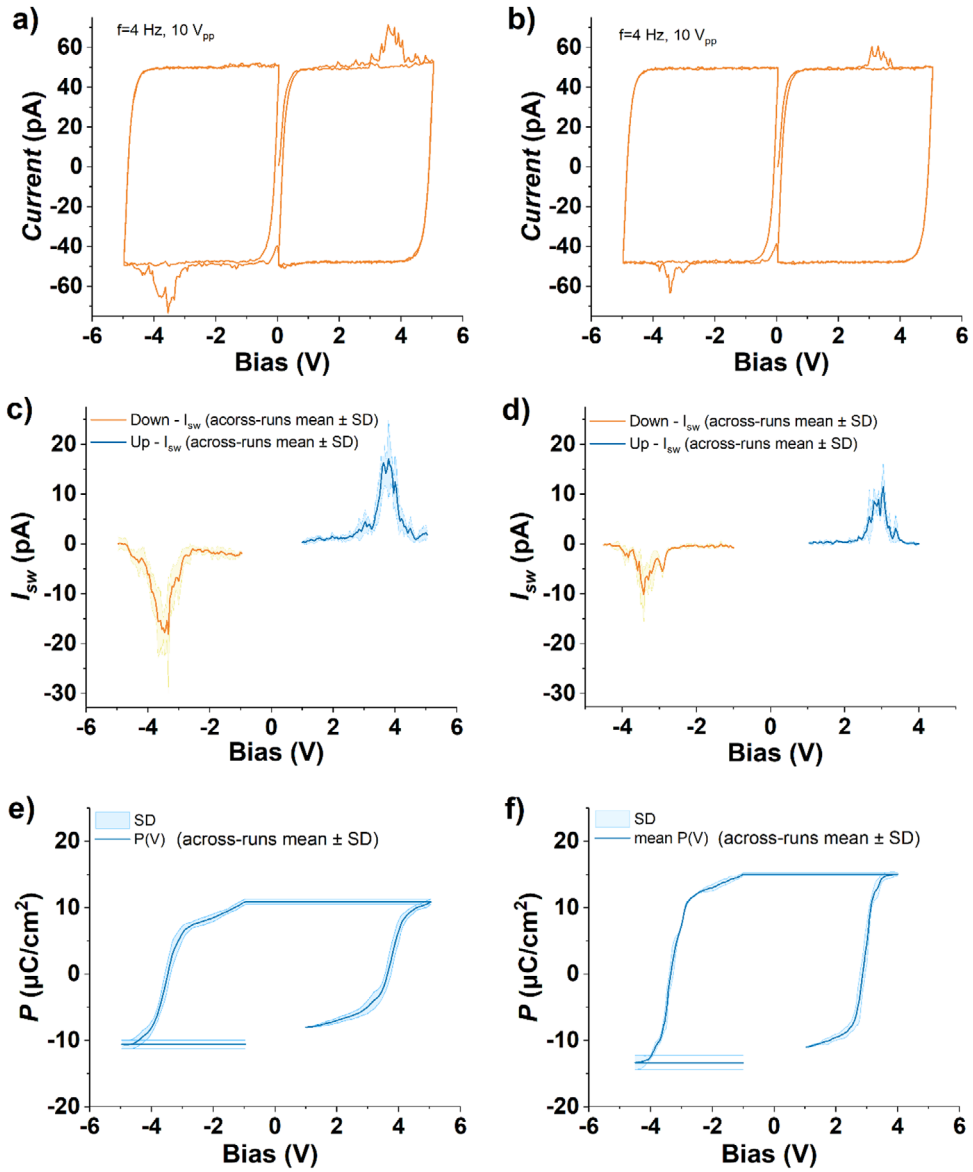

FIGURE 7 | Analysis of ferroelectric switching using PUND measurements for scaled capacitors. Left column: 1.03 μm^2 capacitor; right column: 0.26 μm^2 capacitor. (a,b): measured *I–V* curves from the PUND protocol. (c,d) background-subtracted switching current I_{sw}; (e,f) reconstructed *P–V* hysteresis loops obtained by integrating I_{sw}. *Note: $2P_r$ values and error band represent the mean ± SD across repeated PUND cycles on a representative device ($n = 7$ for 1.03 μm^2; $n = 4$ for 0.26 μm^2).*

remanent states and aggregated across runs as mean ± SD. Using the experimentally determined capacitors area, we find for 1.03 μm^2 capacitor the $2P_r = 20.86 \pm 0.83$ μC·cm^{-2} (SD, $n = 7$); 95% CI: ± 0.76, and for the 0.26 μm^2 capacitor $2P_r = 27.64 \pm 1.19$ μC·cm^{-2} (SD, $n = 4$); 95% CI: ± 1.90. This yields $\Delta(2P_r) \approx 6.78 \pm 1.45$ μC·cm^{-2} (SD combined in quadrature). Across-run $2P_r(V)$ curves are reported as mean ± SD, consistent with between-run variability. Although total switching charge Q_{sw} decreases with area, the normalized $2P_r = Q_{sw}/A$ increases for the smaller capacitor, consistent with edge-dominated switching at elevated perimeter-to-area ratios; given the limited set of lateral geometries, we emphasize the qualitative nature of this attribution. In the (Note S4), we additionally report single-cycle $2P_r$ for a representative loop, defined as the cycle whose $2P_r$ is closest to the across-run mean (i.e., the mean across all cycles within the same run). together with single-run uncertainty obtained by propagating the integration noise at P_r^+ and P_r^- and including the electrode-area contribution in quadrature.

This observation is somewhat counterintuitive since polarization is generally thought to be an intrinsic property of bulk material. This behavior can be attributed to edge effects, where fringing fields near the electrode perimeter enhance the local electric field (E_{local}), creating a boundary region with highly efficient switching kinetics. This intensified E_{local} induces switching of an excess charge (Q_{edge}) from an effective switching area (A_{eff}) that extends beyond the nominal electrode area (A). As the device area shrinks, the Perimeter- to- Area (P/A) ratio increases dramatically, causing the non-scaling perimeter-related charge (Q_{edge}) to become a dominant fraction of the total measured Q_{sw}. When this total charge is normalized by nominal area A,

the result is an apparent enhancement of polarization density, confirming that the increased $2P_r$ is an extrinsic size effect caused by geometric field crowding. Even though the electrode thickness decreases from 22 nm (1.03 μm^2 device) to 16 nm (0.26 μm^2 device), as evidenced by the AFM topography line-profile cross sections, the expected electrical impact of this reduction would be opposite to the observed trend: a thinner W electrode would increase the sheet resistance and degrade lateral potential uniformity, thereby suppressing switching efficiency and typically reducing $2P_r$. In contrast, our measurements show an increase in effective polarization for the smaller devices. A similar scaling behavior has been reported for HfO_2 MIM capacitors, where an area- perimeter model separates bulk and edge current components, with edge contributions becoming dominant as device size decreases [27]. This analogy supports the interpretation that deviations from ideal area scaling originate from geometric field-distribution effects common to dielectric and ferroelectric structures.

In the present study, the evidence for edge-dominated switching is semi-quantitative, as the limited set of lateral geometries does not permit the extraction of a quantitative perimeter-to-area scaling law. Although internal statistics confirm local reproducibility, rigorous quantification will require an expanded device set and dedicated control structures. Local material variations and edge irregularities may further introduce uncertainty in estimating the edge contribution. Despite a possible systematic overestimation of $2P_r$ due to the geometric field crowding, both *I–V* and PUND measurements consistently support the robustness of C-AFM for probing nanoscale ferroelectric switching. A fully quantitative separation of bulk and edge contributions would require additional device geometries and dedicated electrostatic simulations, which lie outside the scope of this methodological study.

3 | Conclusions

This work demonstrates that conductive atomic force microscopy as an effective approach for probing ferroelectric behavior in W/ $Hf_{0.5}Zr_{0.5}O_2$/p-Ge capacitors, demonstrating its applicability across electrode sizes ranging from several micrometers down to 500 nm. C-AFM current mapping and *I–V* spectroscopy, supported by XPS, show that local conductivity correlates with the tungsten surface chemistry, but these variations have a minor impact on the overall switching behavior. Lateral scaling analysis shows that the normalized remnant polarization increases in smaller capacitors, contrary to expectations that remnant polarization is a material property. While this is true for large-area devices, size effects dominate in scaled devices, suggesting that the apparent enhancement originates from edge-dominated switching, where fringing electric fields at the electrode perimeter promote locally intensified polarization reversal that contributes to a non-scaling charge component. Our results highlight both the benefits and limitations of ferroelectric switching devices at the nanoscale. As lateral dimensions decrease, switching current peaks rapidly diminish, while the capacitive current remains constant at about 40 pA, due to parasitic capacitances. Although the 0.26 μm^2 capacitor still exhibits measurable current peaks of ~ 8 pA, in the smallest devices (0.01 μm^2) the ferroelectric switching currents fall below the measurement threshold, completely masked by parasitic capacitances. This defines the practical sensitivity limit of the C-AFM approach and highlights the need for future developments in low-capacitance probe designs and advanced background-subtraction schemes to enable reliable ferroelectric readout.

Beyond reproducing realistic device operation, C-AFM provides spatially resolved insight into the coupling between intrinsic ferroelectric switching and extrinsic structural factors, such as electrode oxidation and geometry, effects that are averaged out in conventional macroscopic measurements. It is worth emphasizing that although C-AFM is a local probing is quite effective in waking up the device by field cycling, and that local switching of the device induces switching in every point of the entire capacitor area, which is beneficial for the operation in real applications. This capability to decouple and evaluate local switching mechanisms establishes C-AFM as a powerful, device-relevant methodology, essential for guiding the scaling and optimization of future ferroelectric memory and neuromorphic architectures.

4 | Experimental Section

HZO films were prepared by plasma-assisted atomic oxygen deposition in a molecular beam epitaxy (MBE) chamber at 80°C on single-crystal p-type Ge(100) substrates (0.013–0.014 Ω·cm). Substrates were pre-annealed at 500°C for 5 min in ultra-high vacuum (UHV) to remove surface contaminants. In situ Reflection High Energy Electron Diffraction (RHEED) was used with an electron energy of 15 keV and an incident angle of 4° recorded in a fluorescent screen.

During HZO growth, Zr and Hf were co-evaporated with equal rates (~ 0.1 Å·s^{-1}) from electron-beam evaporators while a remote RF plasma source (350 W) supplied atomic oxygen at a partial O_2 pressure of 1×10^{-8} mbar. After deposition, 30 nm-thick W top electrodes were patterned by photolithography into circular shapes with a diameter of 10 μm. Smaller electrodes were defined by Electron Beam Lithography (EBL) as squares with lateral sizes of 1, 0.5, and 0.1 μm. To enable lift-off of the electrodes, the samples were spin-coated with a bilayer of MMA/PMMA and exposed in a 100 keV EBL writer. After development in MIBK:IPA 1:2, 30 nm of tungsten was deposited by sputtering, and the resist was removed in acetone.

To crystallize the initially amorphous HZO into the ferroelectric orthorhombic phase, rapid thermal annealing was performed at 420°C for 400 s with a heating ramp of 150°C/s in N_2 atmosphere. The XPS investigations were conducted both in situ and ex situ.

The in situ measurements were performed on the HZO layer, while the ex-situ analysis was carried out on the HZO layer after tungsten electrode deposition. The in-situ measurements were conducted using a SPECS XPS system equipped with a non-monochromatic magnesium Kα X-ray source (photon energy: 1253.6 eV), operated at 12 kV and 12 mA, delivering a total power of 144 W. The photoelectrons were analyzed using a Phoibos 100 mm hemispherical energy analyzer (SPECS GmbH) at a pass energy of 7 eV to ensure high energy resolution. A fixed take-off angle of 54° (relative to the sample surface normal) was used during acquisition. The base pressure in the analysis chamber was maintained below 1×10^{-8} mbar.

For the ex-situ analysis, a Kratos XPS Axis Ultra DLD setup was employed, equipped with a monochromatized Al Kα X-ray source (1486.74 eV) operating at a total power of 180 W, achieved by applying a voltage of 15 kV and a current of 12 mA. The photoelectron analyzer employed in this study was a concentric hemispherical analyzer with a radius of 165 mm. The electron take-off angle was 45°, and it operated in a fixed analyzer transmission mode. The pass energy was established at 20 eV, and a magnetic immersion lens was utilized to augment the efficacy of electron detection. The base pressure of the spectrometer was around 1×10^{-9} mbar. To mitigate the impacts of charging, an electron flood gun was utilized. This gun functioned at an electron energy of 1 eV and an electric current of 0.1 mA. The C 1s peak at 284.6 eV was used as a reference for surface carbon contamination.

Scanning Electron Microscopy (SEM) images were recorded using a Field Emission Scanning Electron Microscope, Gemini 500, from Carl Zeiss Company, Germany. SEM imaging was performed using the InLens detector, operating at an accelerating voltage of 1.5 kV, a working distance of 2.7 mm, and 50 kX magnification.

Conventional electrical measurements were performed on large-area capacitors using an aixACCT TF Analyzer 1000 ferroelectric thin-film tester and tungsten (W) probes. *P–V* loops and switching-current traces were acquired at 1 kHz. The applied voltage sweep was typically ± 2 V. The wake-up of the HZO layer was induced by 1000 electrical cycles at 2 V, with the cycling amplitude chosen slightly below the subsequent read-out sweep (e.g., 2 V cycling preceding a ± 2.5 V read sweep).

Conductive atomic force microscopy (C-AFM) measurements were performed using an MFP-3D SA system (Asylum Research, Oxford Instruments) in ambient air at room-temperature. RMN-25PT300B probes (Rocky Mountain Nanotechnology) with a solid Pt wire tip (nominal radius of ~ 25 nm) and a nominal spring constant of ~ 18 N/m were used. All measurements were carried out under identical force setpoints to ensure consistent tip-sample contact conditions. The C-AFM module Orca, with a sensitivity of 2 nA/V, enabled simultaneous mapping of surface topography and local current. Prior to data acquisition, the tip-sample electrical junction was verified by repeated *I–V* spectroscopy on a platinum reference surface, which yielded highly linear characteristics ($R^2 = 0.999956$), confirming an ohmic and stable interface under the employed experimental conditions (see Note S2 and Figure S7). For C-AFM current mapping, a constant bias of -0.5 V was used with a scan rate of 1 Hz. Local *I–V* spectroscopy was performed by sweeping the voltage at frequencies of 1, 2, 3, and 4 Hz, enabling the analysis of the frequency dependence of the switching behavior. The statistical analysis presented in this work is based on repeated measurements acquired consecutively at the same location on a representative device (1.03 or 0.26 μm^2), thereby minimizing spatial variability and ensuring a stable tip-sample contact during consecutive switching cycles.

Polarization switching was quantified from PUND measurements after correcting the raw current for non-switching contributions. The non-switching baseline current was modeled as $I_{base}(t) = I_0 + G_{eff} \cdot V(t) + C_{par} \cdot (dV/dt)$. Here, C_{par} = 0.60 pF and $G_{eff} = 2.22 \times 10^{-13}$ S were obtained independently from multi-frequency *I–V* measurements, and I_0 was determined from non-switching regions of the voltage sweep. The switching current was then calculated as $I_{sw} = I_{meas} - I_{base}$, and the charge associated with the P and N pulse was obtained by numerical time integration (see Note S7).

To avoid confusion, we use three aggregation levels throughout: (i) local *I–V* ramp averaging (5 consecutive ramps) only for visualization (Figure 3); (ii) across-run PUND statistics for $2P_r$ (1.03 μm^2: $n = 7$; 0.26 μm^2: $n = 4$; Figure 7); and (iii) a representative single-cycle example in the SI. Single-cycle uncertainty propagation details are provided in Note S4 (Figure S10), while the detection-limit analysis (including the numerical I_{LOD}) appears in Note S5.

Acknowledgements

This work was supported by the PNRR project 760239/28.12.2023, funded by the Romanian Ministry of Research, Innovation, and Digitization through the National Recovery and Resilience Plan and the Core Program of the National Institute of Materials Physics under the Project PC2-PN23080202. Funding is also acknowledged from the Horizon Europe projects 101135398 – FIXIT (AD), 101194368 – ViTFOX (AD, LBL), 101135946 CONCEPT (SK, AD) and from the Swiss National Foundation for Science—ROSUBIO #218438 (AF and LB-L). We thank the Binning and Rohrer Nanotechnology Center in Switzerland.

Conflicts of Interest

The authors declare no conflicts of interest.

Data Availability Statement

The data that support the findings of this study are available from the corresponding author upon reasonable request.

References

1. J. F. Scott, *Ferroelectric Memories* (Springer, 2000).

2. V. Garcia and M. Bibes, "Ferroelectric Tunnel Junctions for Information Storage and Processing," *Nature Communications* 5 (2014): 4289, https://doi.org/10.1038/ncomms5289.

3. N. Siannas, C. Zacharaki, P. Tsipas, et al., "Electronic Synapses Enabled by an Epitaxial $SrTiO_{3-\delta}/Hf_{0.5}Zr_{0.5}O_2$ Ferroelectric Field-Effect Memristor Integrated on Silicon," *Advanced Functional Materials* 34 (2024): 2311767, https://doi.org/10.1002/adfm.202311767.

4. T. Francois, L. Grenouillet, J. Coignus, et al., "Impact of Area Scaling on the Ferroelectric Properties of Back-End of Line Compatible $Hf_{0.5}Zr_{0.5}O_2$ and Si:HfO_2-Based MFM Capacitors," *Applied Physics Letters* 118, no. 6 (2021): 062904.

5. W. D. Zhang and A. Q. Jiang, "Size-Scaling Effect on Domain Switching Time and Coercive Field of $TiN/Hf_{0.5}Zr_{0.5}O_2/TiN$ Thin-Film Capacitors," *IEEE Transactions on Electron Devices* 70, no. 12 (2023): 6324–6328.

6. E. Soergel, "Piezoresponse Force Microscopy (PFM)," *Journal of Physics D: Applied Physics* 44 (2011): 464003, https://doi.org/10.1088/0022-3727/44/46/464003.

7. S. V. Kalinin, B. J. Rodriguez, S.-H. Kim, S.-K. Hong, and A. Gruverman, "Imaging Mechanism of Piezoresponse Force Microscopy in Capacitor Structures," *Applied Physics Letters* 92 (2008): 152906, https://doi.org/10.1063/1.2905266.

8. R. K. Vasudevan, N. Balke, P. Maksymovych, S. Jesse, and S. V. Kalinin, "Ferroelectric or Non-Ferroelectric: Why so Many Materials Exhibit

"Ferroelectricity" on the Nanoscale," *Applied Physics Reviews* 4 (2017): 021302, https://doi.org/10.1063/1.4979015.

9. T. Jungk, Á. Hoffmann, and E. Soergel, "Contrast Mechanisms for the Detection of Ferroelectric Domains With Scanning Force Microscopy," *New Journal of Physics* 11 (2009): 033029, https://doi.org/10.1088/1367-2630/11/3/033029.

10. H. Qiao, D. Seol, C. Sun, and Y. Kim, "Electrostatic Contribution to Hysteresis Loop in Piezoresponse Force Microscopy," *Applied Physics Letters* 114 (2019): 152901, https://doi.org/10.1063/1.5090591.

11. N. Balke, P. Maksymovych, S. Jesse, et al., "Differentiating Ferroelectric and Nonferroelectric Electromechanical Effects With Scanning Probe Microscopy," *ACS Nano* 9, no. 6 (2015): 6484–6492.

12. N. Balke, S. Jesse, Q. Li, et al., "Current and Surface Charge Modified Hysteresis Loops in Ferroelectric Thin Films," *Journal of Applied Physics* 118 (2015): 072013, https://doi.org/10.1063/1.4927811.

13. D. Seol, S. Park, O. V. Varenyk, et al., "Determination of Ferroelectric Contributions to Electromechanical Response by Frequency Dependent Piezoresponse Force Microscopy," *Scientific Reports* 6 (2016): 30579, https://doi.org/10.1038/srep30579.

14. A. Fejfar, B. Rezek, and J. Cermak, "Local Current Measurements," in *Quantitative Data Processing in Scanning Probe Microscopy*, ed. P. Klapetek, (Elsevier Inc., 2018), 265–301.

15. N. Schmidt, N. Kaiser, T. Vogel, et al., "Impact of Non-Stoichiometric Phases and Grain Boundaries on the Nanoscale Forming and Switching of HfO_x Thin Films," *Advanced Electronic Materials* 10 (2024): 2300693, https://doi.org/10.1002/aelm.202300693.

16. A. Gomez, "Nano-Positive up Negative Down in Binary Oxide Ferroelectrics," *APL Materials* 12 (2024): 021112, https://doi.org/10.1063/5.0185913.

17. C. Zacharaki, P. Tsipas, S. Chaitoglou, et al., "Very Large Remanent Polarization in Ferroelectric $Hf_{1-x}Zr_xO_2$ Grown on Ge Substrates by Plasma Assisted Atomic Oxygen Deposition," *Applied Physics Letters* 114 (2019): 112901, https://doi.org/10.1063/1.5090036.

18. N. Siannas, C. Zacharaki, P. Tsipas, et al., "Metastable Ferroelectricity Driven by Depolarization Fields in Ultrathin $Hf_{0.5}Zr_{0.5}O_2$," *Communications Physics* 5 (2022): 178, https://doi.org/10.1038/s42005-022-00951-x.

19. C. Zacharaki, S. Chaitoglou, N. Siannas, P. Tsipas, and A. Dimoulas, "$Hf_{0.5}Zr_{0.5}O_2$-Based Germanium Ferroelectric p-FETs for Nonvolatile Memory Applications," *ACS Applied Electronic Materials* 4, no. 6 (2022): 2815–2821, https://doi.org/10.1021/acsaelm.2c00324.

20. G. Wang, Y. Ling, H. Wang, et al., "Hydrogen-Treated WO_3 Nanoflakes Show Enhanced Photostability," *Energy & Environmental Science* 5 (2012): 6180–6187, https://doi.org/10.1039/c2ee03158b.

21. B. A. Deangelis and M. Schiavello, "X-Ray Photoelectron Spectroscopy Study of Nonstoichiometric Tungsten Oxides," *Journal of Solid State Chemistry* 21 (1977): 67–72, https://doi.org/10.1016/0022-4596(77)90145-1.

22. T. H. Fleisch and G. J. Mains, "An XPS Study of the UV Reduction and Photochromism of MoO_3 and WO_3," *The Journal of Chemical Physics* 76 (1982): 780–786, https://doi.org/10.1063/1.443047.

23. S. Ding, J. Jia, B. Xu, et al., "Overrated Energy Storage Performances of Dielectrics Seriously Affected by Fringing Effect and Parasitic Capacitance," *Nature Communications* 16 (2025): 608, https://doi.org/10.1038/s41467-025-55855-5.

24. N. Siannas, C. Zacharaki, P. Tsipas, et al., "Metastable Ferroelectricity Driven by Depolarization Fields in Ultrathin $Hf_{0.5}Zr_{0.5}O_2$," *Communications Physics* 5 (2022): 178.

25. F. P. G. Fengler, M. Hoffmann, S. Slesazeck, T. Mikolajick, and U. Schroeder, "On the Relationship Between Field Cycling and Imprint in Ferroelectric $Hf_{0.5}Zr_{0.5}O_2$," *Journal of Applied Physics* 123 (2018): 204101, https://doi.org/10.1063/1.5026424.

26. M. Rommel, J. D. Jambreck, M. Lemberger, et al., "Influence of Parasitic Capacitances on Conductive AFM I-V Measurements and Approaches for Its Reduction," *Journal of Vacuum Science & Technology B* 31 (2013): 01A108, https://doi.org/10.1116/1.4768679.

27. F. M. Puglisi, P. Pavan, A. Padovani, and L. Larcher, "Perimeter and Area Current Components in HfO_2 and HfO_{2-x} Metal-Insulator-Metal Capacitors," *Journal of Vacuum Science & Technology B* 31 (2013): 01A117.

Supporting Information

Additional supporting information can be found online in the Supporting Information section.

Supporting File: aelm70443-sup-0001-SuppMat.docx.